JOURNAL OF GUIDANCE, CONTROL, AND DYNAMICS
Vol. 31, No. 2, March–April 2008

Model Reduction of Input–Output Dynamical Systems by Proper Orthogonal Decomposition

Arthur C. Or* and Jason L. Speyer†
Mechanical and Aerospace Engineering Department, University of California, Los Angeles, California 90095
and
Henry A. Carlson‡
Clear Science Corporation, Harford, New York 13784

DOI: 10.2514/1.29456

We performed a study using an empirical-based model reduction technique known as balanced proper orthogonal decomposition. The technique, applicable to nonlinear systems, yields a set of basis functions that span a proper orthogonal decomposition-based subspace capturing the essential input–output dynamics structure. Projection of the original model on this subspace yields the balanced reduced-order model. In this study the performance of the balanced reduced-order model is compared with the original high-order linear model, and the dependence on the sampling parameters is studied. Even with a large number of snapshots, we show that at least 52 real states are needed for the balanced reduced-order model to produce good performance. The sampling frequency has to be high enough to cover twice the high-frequency modes of interest. We develop a novel algorithm, which in linear systems is based on a direct decomposition of the discrete Hankel matrix. The algorithm serves as a generalized balanced proper orthogonal decomposition scheme for input–output model reduction. The algorithm is especially efficient for a reduced number of snapshots and it suits nonlinear systems well because the propagation of the adjoint equation is not required. A single sample rate is found to be inadequate to cover both high- and low-end frequencies. To reduce the number of snapshots significantly, we show that *multiple* sampling rates improve performance dramatically.

I. Introduction

A MAJOR motivation for obtaining a balanced reduced-order model (BROM) is for the design of a robust controller for large dynamical systems. Flow control represents an important class of such systems. For examples of these studies, see Joshi et al. [1,2], Mahajan et al. [3], and Carlson et al. [4]. The first two papers deal with spectral methods, and the last two papers deal with finite-difference methods of computational fluid dynamics (CFD) systems. Such a scope is very different from traditional analytical studies, such as deriving evolution-type equations from the Navier–Stokes system using parameter expansion and perturbation technique [5,6]. Significant interests have developed recently in using the empirical approach. This approach also has a long history, traced back to the Karhunen–Loeve expansion [7], more recently known as the proper orthogonal decomposition (POD). For a control application to large dynamical systems, a number of authors have extended the method to applications to input–output systems [8–10].

The empirical method based on the POD performs the order reduction and input–output balance all together. By sampling the flowfields excited by the internal dynamics, the POD-based algorithm basically provides a subspace consisting of a set of POD-based basis functions. The internal dynamics are not excited by arbitrary initial states, but rather by prescribed input forcing. For input–output systems, the empirically generated subspace has to capture the dominant dynamical features. However, there is no guarantee that the controllable and observable modes, upon balancing, will capture all the essential dynamical properties. Our focus of interest is the following: 1) determine the order of this subspace that captures the dominant dynamical features, and 2) determine the projected input–output structure in the subspace that preserves the original input–output structure. So far, there does not seem to be many published analyses on the subject when it comes to input–output systems. For instance, Willcox [8] indicated that the airfoil response force to a pulse plunge input matches very well between the BROM and the CFD model. Therefore, if the input is the plunge pulse and the output is the response force, Willcox's BROM shows good performance. For other types of input–output relationships, however, this model may have no bearing at all. Carlson et al. [4] used the POD technique and demonstrated that a ROM with two leading modes describing the trailing vortex instability in the airfoil captures over 95% of the total flow kinetic energy. In other words, it meets objective one of our focus of interest. However, the results do not appear to be sufficient for capturing major modes that dictate the observability (typically located at the higher frequency band). Lall et al. [9] pioneered applying the POD to nonlinear systems. Again, there is no available example to demonstrate and compare the detailed structure between the ROM and the infinite-dimensional model. Rowley [10] investigated a Poiseuille flow stability problem like ours, but with a different emphasis.

In this study, our goal is to obtain reasonable performance by comparing the BROM with the original high-order model by using as small a number of snapshots as possible. With the frequency band of interest picked to represent the input–output dynamics of interest, we relate the Nyquist frequency and the lowest frequency to the sampling time interval as well as the number of snapshots (samples). A generalized POD scheme that employs the discrete Hankel matrix is provided. The results demonstrate a tradeoff of the computational efficiency (a small number of snapshots) versus performance (matching Bode plots between BROM and the original model). Performance of the BROM depends on the number of reduced states, sample time interval size, and the number of samples (each sample is a snapshot). The sampling parameters ultimately are related to the Nyquist frequency and the lowest modal frequency of interest. To

Received 23 December 2006; revision received 27 August 2007; accepted for publication 17 September 2007.

*Research Associate. Member AIAA.
†Professor. Fellow AIAA.
‡CEO. Member AIAA.

reduce the number of snapshots but to accommodate the whole frequency band, we try sampling the empirical data at multiple rates.

II. Governing Equations for Two-Dimensional Linear Disturbance in a Poiseuille Channel Flow

The two-dimensional plane Poiseuille flowfield stability is described by (u, v, p) where $u(x, y, t)$ and $v(x, y, t)$ are the horizontal and vertical perturbation velocities, respectively, and $p(x, y, t)$ is the pressure perturbation. The perturbations are linearized about a steady mean flow $U(y) = (1 - y^2)$ and U_y denotes its vertical gradient. For an infinite horizontal layer, the perturbation fields are Fourier decomposed according to $u(x,y,t)=\frac{1}{2}u(y,t)\exp(ikx)+\text{c.c.}$, $v(x,y,t)=\frac{1}{2}v(y,t)\exp(ikx)+\text{c.c.}$, and $p(x, y, t) = \frac{1}{2} p(y, t) \exp(ikx) + \text{c.c.}$ (where c.c. denotes complex conjugate. The same notations u, v, and p are used for both field and modal variables to cut down on the number of symbols used). The momentum equations are

$$\begin{aligned} \partial_t u + ikUu + U_y v &= -ikp + \frac{1}{Re}(D^2 - k^2)u, \\ \partial_t v + ikUv &= -Dp + \frac{1}{Re}(D^2 - k^2)v \end{aligned} \tag{1}$$

where k is the wave number along the x direction and D denotes the derivative with respect to y. The flowfield satisfies the incompressible mass conversation equation

$$iku + Dv = 0 \tag{2}$$

The control problem uses pumping and suction at the lower wall as actuation, and so $v(-1, t) = \zeta(t)$ where $\zeta(t)$ is the prescribed control action. The boundary conditions are nonslip on the upper and lower walls, nonpenetration on upper wall, and pumping and suction on the lower wall, respectively,

$$u(\pm 1, t) = 0, \qquad v(1, t) = 0, \qquad v(-1, t) = \zeta(t) \tag{3}$$

The mass constraint is automatically satisfied by defining the stream function $\phi(y, t)$ according to $\mathbf{u} = \nabla \times (\mathbf{k}\phi)$, where $\mathbf{u} = (u, v, 0)$ is the perturbation velocity and $\mathbf{k}$ is the unit vector along the z axis. In scalar form, we have

$$\begin{bmatrix} u \\ v \end{bmatrix} = \begin{bmatrix} D \\ -ik \end{bmatrix} \phi \tag{4}$$

Substituting u, v for ϕ in Eq. (1), we cross differentiate the two equations to eliminate pressure. The resulting equation is the well-known Orr–Sommerfeld equation:

$$(\partial_t + Uik)(D^2 - k^2)\phi - ikU_{yy}\phi = \frac{1}{Re}(D^2 - k^2)^2\phi \tag{5}$$

ϕ is subjected to the boundary conditions

$$D\phi(\pm 1, t) = 0, \qquad \phi(1, t) = 0, \qquad -ik\phi(-1, t) = \zeta(t) \tag{6}$$

For most of the results presented, the measurement is the shear stress at the lower wall, $\tau_w(t) = \frac{1}{Re}(Du(y, t)|_{y=-1} + ikv(-1, t))$, so

$$\tau_w(t) = \frac{1}{Re}(D^2 + k^2)\phi(y, t)|_{y=-1} \tag{7}$$

The Orr–Sommerfeld equation gives $\phi(y, t)$, which in turn determines the velocity field by Eq. (4).

The above infinite-dimensional system can be converted to the finite standard state-space form. A detailed description of the conversion methods based on the spectral techniques can be found in Or et al. [11].

III. POD-Based Empirical Balanced Order Reduction

The algorithm presented here can be viewed as an extended version that generalizes those presented in Lall et al. [9], Willcox and Peraire [8], and Rowley [10]. The algorithm can be adapted to be used directly for the nonlinear partial differential systems. The treatment of the controllability Gramian is straight forward. The subtlety is in the treatment of the observability Gramian. This algorithm is primarily designed for the use of nonlinear systems and for this reason the adjoint equation is not required.

A. Development of the Controllability Gramian

Consider the input controls to be a time-delta function with a spatial shape compatible with the disturbance mode shape. These control inputs should be rich enough to stimulate the nonlinear partial differential system representing the flowfield.

The sampled outputs probe the internal state of the dynamics. These can be the velocity field at grid points for the momentum equations or the stream function field for the Orr–Sommerfeld equation. In the case of the spectral decomposed system, these can be the Chebyshev–Fourier coefficients of the corresponding fields. Furthermore, to reduce the dimension we treat the complex field. A set of snapshots are collected in time $t_1, t_2, \ldots, t_{m_c}$. The snapshots due to the control impulses are represented as the controlled data matrix

$$\begin{aligned} &\mathcal{X} \\ &= [\mathbf{x}_1(t_1), \ldots, \mathbf{x}_1(t_{m_c}), \ldots, \mathbf{x}_2(t_1), \ldots, \mathbf{x}_2(t_{m_c}), \ldots, \mathbf{x}_p(t_1), \ldots, \mathbf{x}_p(t_{m_c})] \end{aligned} \tag{8}$$

where p is the number of control inputs and the response to each control is applied separately; $\mathbf{x}(t_j) = [\mathbf{x}_i(t_j), i = 1, \ldots, p]$ is an N-dimensional vector and N is the number of physical grid points or the number of modal coefficients for each control impulse. Therefore, $\mathcal{X}$ is an $N \times m_c p$ matrix. The number of snapshots depends on the frequency band that is to be captured. At the high-frequency end, the sample rate is dictated by the Nyquest criterion. At the low-frequency end, the sampled time interval must be large enough to capture the slowest modes. These extremes dictate the number of samples or snapshots needed. If $m_c p \gg N$, then the method of Lall et al. [9] is appropriate. If $m_c p \ll N$, then the method to be described is computationally efficient. The latter case is the focus of the paper.

From the controlled data matrix, we form a correlation matrix $\mathbf{R}_c = \mathcal{X}\mathcal{X}^+$ (the superscript + denotes the transpose of the complex conjugate).Consider a linear dynamical system $\mathbf{x}(t_j) = \mathbf{\Phi}(t_j, t_0)\mathbf{B}$, where $\mathbf{\Phi}(t_j, t_0)$ is the transition matrix. Note that, due to the initial impulse control, the solution is the result of using the $N \times p$ input matrix $\mathbf{B}$ as the initial condition into the unforced dynamical system [10]. Furthermore, the correlation matrix $\mathbf{R}_c$ can be written as

$$\mathbf{R}_c = \mathcal{X}\mathcal{X}^+ = \sum_{i=1}^{p}\sum_{j=1}^{m_c} \mathbf{x}_i(t_j)\mathbf{x}_i^+(t_j) = \sum_{j=1}^{m_c} \mathbf{\Phi}(t_j, t_0)\mathbf{B}\mathbf{B}^+\mathbf{\Phi}(t_j, t_0)^+ \tag{9}$$

This correlation matrix $\mathbf{R}_c$ is an empirical, finite, and time-discrete version of the $N \times N$ controllability Gramian $\mathbf{W}_c$.

Next we consider constructing the eigenvalues and eigenvectors for $\mathbf{R}_c$. Note that, for the Hermitian matrix $\mathbf{R}_c$, the eigenvalues are nonnegative and equal to the singular values. The rank of $\mathbf{R}_c$ is $N_a \le m_c p$. The eigenvectors are the basis vectors in the singular-value decomposition. First, we determine the N-dimensional eigenvectors $\mathbf{v}_{c_j}$, associated with the positive eigenvalues of $\mathbf{R}_c$,

$$\mathbf{R}_c\mathbf{v}_{c_j} = \mathcal{X}\mathcal{X}^+\mathbf{v}_{c_j} = \lambda_j\mathbf{v}_{c_j}, \qquad j = 1, \ldots, N_a \tag{10}$$

In the algorithms commonly used, alternatively, a set of $m_c p$-dimensional eigenvectors $\mathbf{u}_{c_j}$ can be constructed as

$$\mathcal{X}^+\mathcal{X}\mathbf{u}_{c_j} = \lambda_j\mathbf{u}_{c_j}, \qquad j = 1, \ldots, N_a \le m_c p \tag{11}$$

The eigenvalues λ_j are the same in Eqs. (10) and (11). The relationship between the eigenvectors $\mathbf{v}_{c_j}$ and $\mathbf{u}_{c_j}$ are obtained if Eq. (11) is multiplied on the left by $\mathcal{X}$ as

$$(\mathcal{X}\mathcal{X}^{+})\mathcal{X}\mathbf{u}_{c_j} = \lambda_j \mathcal{X}\mathbf{u}_{c_j}, \qquad j = 1, \ldots, N_a \le m_c p \tag{12}$$

Comparing the previous equation with Eq. (10) and choosing $\mathbf{u}_{c_j}$ to be orthonormal, then

$$\mathbf{v}_{c_j} = \mathcal{X}\mathbf{u}_{c_j}/\sqrt{\lambda_j} \tag{13}$$

where the orthonormal condition gives

$$\mathbf{v}_{c_j}^{+}\mathbf{v}_{c_j} = \mathbf{u}_{c_j}^{+}\mathcal{X}^{+}\mathcal{X}\mathbf{u}_{c_j}/\lambda_j = \mathbf{u}_{c_j}^{+}\mathbf{u}_{c_j} = 1 \tag{14}$$

B. Observability Gramian and the Decomposition of the Hankel Matrix

The normalized basis vectors $\mathbf{v}_{c_k}$ are introduced into the partial differential system as initial conditions. These bases form a subspace associated with the dominant controllability eigenvalues. Let the dimension of this subspace be $N_c \le N_a \le m_c p$, where N_c represents the dominate eigenvalues of the controllability Gramian. The outputs from the measurement equation $\mathbf{y}_k(t_j) = \mathbf{C}\mathbf{x}_k(t_j)$ ($\mathbf{C}$ is a $q \times N$-dimensional output matrix), where $\mathbf{y}_k(t_j)$, $k = 1, \ldots N_c$, $j = 1, \ldots, m_o$ are propagated for each initial condition $\mathbf{v}_{c_k}, k = 1, \ldots N_c$, where $\mathbf{x}_k(t_j) = \mathbf{\Phi}(t_j, t_0)\mathbf{v}_{c_k}$ and recorded as a set of snapshots for times $t_1, t_2, \ldots t_{m_o}$. The elements of output $\mathbf{y}_k(t_j)$ are the outputs $y_{ik}(t_j)$ (where $i = 1, \ldots, q$, $k = 1, \ldots, N_c$, and $j = 1, \ldots, m_o$) and are related to linear theory as

$$[\mathbf{Y}_1, \ \ldots, \ \mathbf{Y}_{N_c}] = \begin{bmatrix} y_{11}(t_1) & \ldots & y_{1N_c}(t_1) \\ \vdots & \vdots & \vdots \\ y_{11}(t_{m_o}) & \ldots & y_{1N_c}(t_{m_o}) \\ y_{12}(t_1) & \ldots & y_{2N_c}(t_1) \\ \vdots & \vdots & \vdots \\ y_{21}(t_{m_o}) & \ldots & y_{2N_c}(t_{m_o}) \\ \vdots & \vdots & \vdots \\ y_{q1}(t_1) & \ldots & y_{qN_c}(t_1) \\ \vdots & \vdots & \vdots \\ y_{q1}(t_{m_o}) & \ldots & y_{qN_c}(t_{m_o}) \end{bmatrix} \begin{bmatrix} C_1\mathbf{\Phi}(t_1, t_0) \\ \vdots \\ C_1\mathbf{\Phi}(t_{m_o}, t_0) \\ C_2\mathbf{\Phi}(t_1, t_0) \\ \vdots \\ C_2\mathbf{\Phi}(t_{m_o}, t_0) \\ \vdots \\ C_q\mathbf{\Phi}(t_1, t_0) \\ \vdots \\ C_q\mathbf{\Phi}(t_{m_o}, t_0) \end{bmatrix} [\mathbf{v}_{c_1} \ \cdots \ \mathbf{v}_{c_{N_c}}] \tag{15}$$

where $\mathbf{C}$ is a $q \times N$ matrix. The data matrix of $y_{ik}(t_j)$ has the dimension $m_o q \times N_c$.

Note that $\mathbf{Y}_i$ is related to the observability Gramian the following way:

$$\mathbf{Y}_i^{+}\mathbf{Y}_j = \mathbf{v}_{c_i}^{+}\left\{\sum_{j}^{m_o} \mathbf{\Phi}(t_j, t_0)^{+}\mathbf{C}^{+}\mathbf{C}\mathbf{\Phi}(t_j, t_0)\right\}\mathbf{v}_{c_j} = \mathbf{v}_{c_i}^{+}\mathbf{W}_o\mathbf{v}_{c_j} \tag{16}$$

We denote $\mathbf{Y} = [\mathbf{Y}_1, \ldots, \mathbf{Y}_{N_c}]$. Then, $\mathbf{Y}^{+}\mathbf{Y} = \mathbf{V}^{+}\mathbf{W}_o\mathbf{V}$, where $\mathbf{V} = [\mathbf{v}_{c_1} \ \cdots \ \mathbf{v}_{c_{N_c}}]$ is $N \times N_c$ and $\mathbf{V}^{+}\mathbf{V} = \mathbf{I}$.

Rather than reducing $\mathbf{V}^{+}\mathbf{W}_o\mathbf{V}$, we follow the result of Rowley [10] and exploit the structure of $\mathbf{Y}$ instead. From Eq. (15) note that the observed data matrix, denoted by $\mathcal{Y}^{+}$ (which can also be obtained by sampling the propagating adjoint state equation), is contained in the first matrix on the right-hand side of Eq. (15). Equation (15) is denoted as

$$\mathbf{Y} = \mathcal{Y}^{+}\mathbf{V} \tag{17}$$

where the empirical version of the observability Gramian $\mathbf{W}_o$ is given by $\mathbf{R}_o = \mathcal{Y}\mathcal{Y}^{+}$. However, from Eq. (13), $\mathbf{V}$ is related to $\mathbf{U} = [\mathbf{u}_{c_1}, \ldots, \mathbf{u}_{c_{N_c}}]$ as $\mathbf{V} = \mathcal{X}\mathbf{U}\mathbf{\Lambda}^{-1/2}$, where the last is a diagonal matrix consisting of entries λ_i. Equation (17) becomes

$$\mathbf{Y} = (\mathcal{Y}^{+}\mathcal{X})\mathbf{U}\mathbf{\Lambda}^{-1/2}$$

Inverting the equation gives

$$\mathcal{Y}^{+}\mathcal{X} = \mathbf{Y}\mathbf{\Lambda}^{1/2}\mathbf{U}^{+} \tag{18}$$

The quantity on the left-hand side, $\mathcal{Y}^{+}\mathcal{X}$, is the discrete form of the Hankel matrix with the dimension $m_o q \times N_c$, the size of the snapshots for the control and the measurements, not the size of the internal states. Because $\mathbf{Y}$, $\mathbf{U}$, and $\mathbf{\Lambda}$ are known, this quantity can be obtained. This algorithm does not require us to provide the measurement matrix $\mathbf{C}$ [see Eq. (15) explicitly], as required when using the adjoint equation. In the CFD-based model, the discrete Hankel matrix can be computed via the measured data rather than via model data.

Following Rowley [10], we decompose $\mathcal{Y}^{+}\mathcal{X}$ to determine the balanced POD basis functions as

$$\mathcal{Y}^{+}\mathcal{X} = \tilde{\mathbf{U}}\mathbf{\Sigma}\tilde{\mathbf{V}}^{+} = [\tilde{\mathbf{U}}_1 \ \ \tilde{\mathbf{U}}_2]\begin{bmatrix} \mathbf{\Sigma}_1 & 0 \\ 0 & 0 \end{bmatrix}\begin{bmatrix} \tilde{\mathbf{V}}_1^{+} \\ \tilde{\mathbf{V}}_2^{+} \end{bmatrix} = \tilde{\mathbf{U}}_1\mathbf{\Sigma}_1\tilde{\mathbf{V}}_1^{+} \tag{19}$$

where the dimension of $\mathbf{\Sigma}_1$ is $r \times r$ and r is essentially the rank of the discrete Hankel matrix $\mathcal{Y}^{+}\mathcal{X}$. $\mathbf{\Sigma}_1$ can be decomposed even further if only the largest singular values in $\mathbf{\Sigma}_1$ are retained in constructing the balanced POD basis functions. As given in Eq. [10], the POD modes are given by $\mathcal{P}$ (with dimension $N \times r$), where

$$\mathcal{P} = [\tilde{\mathbf{p}}_1, \ldots, \tilde{\mathbf{p}}_r] = \mathcal{X}\tilde{\mathbf{V}}_1\mathbf{\Sigma}_1^{-1/2} \tag{20}$$

For linear systems, the partial differential system corresponds to the state space $(\mathbf{A}, \mathbf{B}, \mathbf{C})$ with the N-dimensional state vector $\mathbf{x}$. Then, the reduced-order state-space system with r-dimensional state vector $\mathbf{x}_r$ is given by

$$\dot{\mathbf{x}}_r = (\mathcal{P}^{\#}\mathbf{A}\mathcal{P})\mathbf{x}_r + (\mathcal{P}^{\#}\mathbf{B})\mathbf{u}, \qquad \mathbf{y} = (\mathbf{C}\mathcal{P})\mathbf{x}_r \tag{21}$$

where $\mathcal{P}^{\#}$ is the pseudoinverse of $\mathcal{P}$. Note that $\mathcal{P}^{\#}\mathbf{B}$ and $\mathbf{C}\mathcal{P}$ are a balanced form.

If the adjoint equation is available [10], we can integrate $(\mathbf{A}^{+}, \mathbf{C}^{+})$ in the same way as $(\mathbf{A}, \mathbf{B})$, which yields the observed data matrix $\mathcal{Y}$:

$$\mathcal{Y} = [\mathbf{x}_1(t_1), \ldots, \mathbf{x}_1(t_{m_o}), \ldots, \mathbf{x}_2(t_1), \ldots, \mathbf{x}_2(t_{m_o}), \ldots, \mathbf{x}_q(t_1), \ldots, \mathbf{x}_q(t_{m_o})] \tag{22}$$

Although the method presented is justified in terms of a linear system, the motivation in creating this method is that it is applicable to nonlinear systems in a heuristic sense. However, because superposition is not valid for nonlinear systems, the number of control combinations in Eq. (8) should be made richer by putting in various combinations of the controls.

IV. Results

We begin by addressing the two main sampling parameters: the number of snapshots, N_c (equal to N_o); and the number of integrated time steps between successive samples, N_i. It becomes clear that N_c is related to the lowest frequency of interest, f_0, and N_i is related to the highest frequency of interest, f_1, in the input–output transfer functions. The sampling frequency, f_s (Hz), is twice the highest frequency of interest, which is the Nyquist cutoff frequency, f_c (Hz). The sampling interval is $N_i\Delta t$ (where Δt is the integration time step). From the Nyquist frequency $f_c = (2N_i\Delta t)^{-1}$, the number of samples are $N_c = f_s/(f_0/2) = 2(N_i f_0 \Delta t)^{-1}$. Take, for example, the lowest frequency at $Re = 10^4$ and $k = 1$, $f_0 = 0.237/(2\pi) = 0.0377$. Let the time step $\Delta t = 0.01$. It is determined that the best sampling interval is below $3\Delta t$. For $N_i = 3$, $f_s = 1/(3\Delta) = 33.33$, the Nyquist frequency, $f_c = 16.67$ and the number of snapshots is $2f_s/f_0 = 1767$. Therefore, around 2000 snapshots are required.

We will first show some numerical results at this large number of snapshots to establish the best performance possible with the empirical algorithm. After this, we will focus on developing a sampling scheme that uses as few snapshots as possible while maintaining a decent performance. For this purpose, multiple sampling interval sizes will be used to cover the low- as well as the high-frequency bands.

Table 1 First three poles at the critical point $k = 1.02$, $Re = 5772.22$ in the state-space model

NT	First pole	Second pole	Third pole
16	0.0122479812 − 0.2767468227i	−0.0149461215 − 0.335789765i	−0.017587466 − 0.94199991i
32	8.12019628e − 07 − 0.269202225i	−0.0462116529 − 0.97243526i	−0.0591957158 − 0.327427817i
64	−5.83647376e − 08 − 0.269215086i	−0.0466573001 − 0.972972137i	−0.0587615364 − 0.327639470i
128	−3.14544188e − 07 − 0.269215119i	−0.0466929831 − 0.97299626i	−0.0587616280 − 0.32763953i

It is worth noting how the leading eigenvalues are affected by the truncation effects of the original model. Table 1 shows the first three eigenvalues at the critical point (determined to be approximately $k = 1.02$ and $Re = 5772.22$). The result in Table 1 suggests that 16 Chebyshev modes are insufficient. However, a convergent trend is evident from 32 to 128 complex modes. The order of the states is doubled by converting the complex to the real system. The eigenvalues in the real system are in complex conjugate pairs [see Eq. (23)]. Next, we compare the neutral stability boundary in the wave number–Reynolds number (the so-called neutral curve) between the original model and the BROM of 26 complex modes. The dashed curve in Fig. 1 represents the theoretical boundary based on the linear theory that separates the stable (below the curve) from the unstable region (above the curve). The critical point is approximately determined to be $k = 1.02$ and $Re = 5772.22$. For each wave number k, we perform the model reduction for several Reynolds numbers that span the stable and unstable ranges, then we interpolate the data to obtain a crossover value of Re for k. This produces the solid curve (the data points are marked by ○ in the figure). A very good match between the neutral curve of the BROM and the theoretical curve is obtained for the two branches a significant distance from the critical-point minimum region. There is quite a bit of distortion near the critical point. We conclude that the BROM captures the linear stability boundary with some distortion in the region of the critical point.

To show whether the POD basis functions form a subspace in which the projections of the input and output vectors adequately retain the original structure, we have to turn to comparing the input-to-output transfer functions. It appears that for physical interpretations the gain-phase plots in the frequency domain are the easiest choice. However, we have to convert the complex state space to the real state space. For any complex vector or matrix $\mathbf{a}$, the conversion is

$$\mathbf{a} \rightarrow \begin{bmatrix} \mathrm{Re}(\mathbf{a}) & \mathrm{Im}(\mathbf{a}) \\ \mathrm{Im}(\mathbf{a}) & \mathrm{Re}(\mathbf{a}) \end{bmatrix} \tag{23}$$

The real system has doubled the dimensions of the complex system. A complex single-input, single-output system becomes a two-inputs, two-outputs system. We show only the case for $k = 1.0$ and $Re = 10^4$, because results near the critical point are found to be sufficiently similar. We use $\Delta t = 0.0075$, $N_i = 3$, which gives a sampling interval of about 0.2. We use a large number of snapshots, with $N_c = N_0 = 2000$. These sampling parameters gives $f_0 = 0.038$ Hz and $f_c = 22.2$ Hz. Figure 2 compared the Bode plots for the gain (dB) and phase (deg) between the original model (256 real states, $NT = 128$) and the BROM (52 real states, $N_r = 26$). The Bode plots show a frequency range from 10^{-1} to 10^{1}. The left column shows the in-channel (input-to-output: 1-to-1 or 2-to-2) gain and phase plots and the right column shows the cross-channel (input-to-output: 1-to-2 or 2-to-1) gain. The solid curves represent the BROM model and the dashed curves represent the original model. The gain-phase curves visually overlap those of the original model. The resonance peak occurs at $f = 0.038$ Hz. Note that the in-channel versus cross-channel gains behave quite differently at higher frequencies. The in-channel gain has a roll off but the cross-channel gain appears to settle at a constant value. The different behavior is due to the fact that the shear stress measurement has the same phase as the stream function, which has a 90 deg complex phase shift from the control quantity, which is the pumping-and-suction velocity. Both quantities are evaluated at the lower wall.

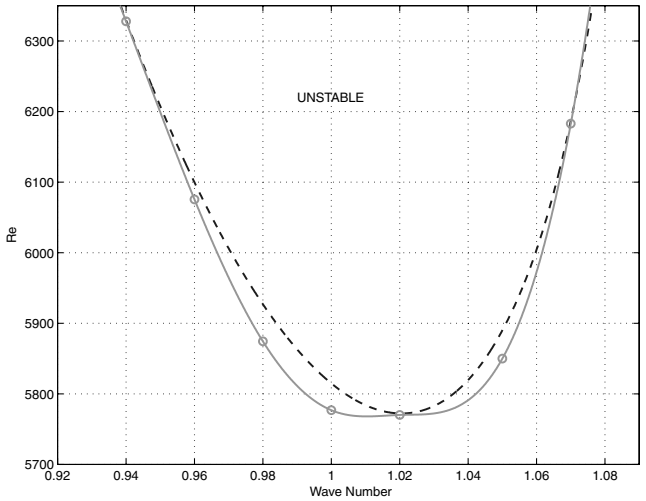

Fig. 1 Neutral stability curve: theoretical (dashed) and empirical (solid).

We demonstrate that, for large number of snapshots, the BROM adequately captures the input–output transfer functions of the original model. However, the performance starts to deteriorate if we reduce the number of states. We are convinced that 26 POD modes are required to resolve the controllability and observability structures, and these structures require modes of high-frequency content, so that is the reason we require 26 modes. However, for computational efficiency, the number of snapshots to be processed posts significant constraints. Hereafter, we investigate how to reduce the number of snapshots but maintain reasonable performance.

We have run a large number of pole-zero maps and Bode plots of the BROM, by keeping the original model at $Re = 10^4$ and $k = 1$ and $NT = 128$, but varying the sampling parameters, the sampling interval $N_i\Delta$, and the number of snapshots $N_c = N_0$. Finally, while maintaining the same overall number of snapshots, two sampling intervals were used, one short and one long, to capture high and low frequencies. We describe our finding qualitatively as follows. First, we varied the sampling interval size from 0.01 to 0.3 and found little change in the Bode plots. It is crucial that we pick a sampling interval so that the Nyquist frequency covers the high-frequency dynamics modes of interest, but the data set is long enough to capture the lower frequencies.

The resonance peak is at 0.038 Hz. The imaginary parts of the poles and the zeros of the original model are bounded by 1 Hz. The real parts, however, extend to negative infinity. When we refer to the sampling frequency and the high-frequency modes, we refer to the frequency domain of the Bode plots. At first glance, we anticipated that a large sampling interval would capture the low-frequency dynamics and would use fewer snapshots. However, we observe that the gain-phase plots start to deteriorate significantly at as soon as the sampling interval size exceeds, say, 0.05, after which improvement is unlikely even if more snapshots are used. Further, the deterioration is not restricted to the higher-frequency behavior, but also extends to the low-frequency gain and phase values and is especially bad in the cross-channel Bode plots. One characterization of the reduced-order model properties is provided by the pole-zero structure near the imaginary axis. This region exhibits sensitivity to the sampling interval size. When the sampling interval size is too large or there are not enough snapshots, we observe a significant sensitivity of the poles and the number of zeros, as well as their locations near the imaginary axis of the s plane. An extra pair of poles or numerous pairs of zeros can cross to the right-hand side of the s plane.

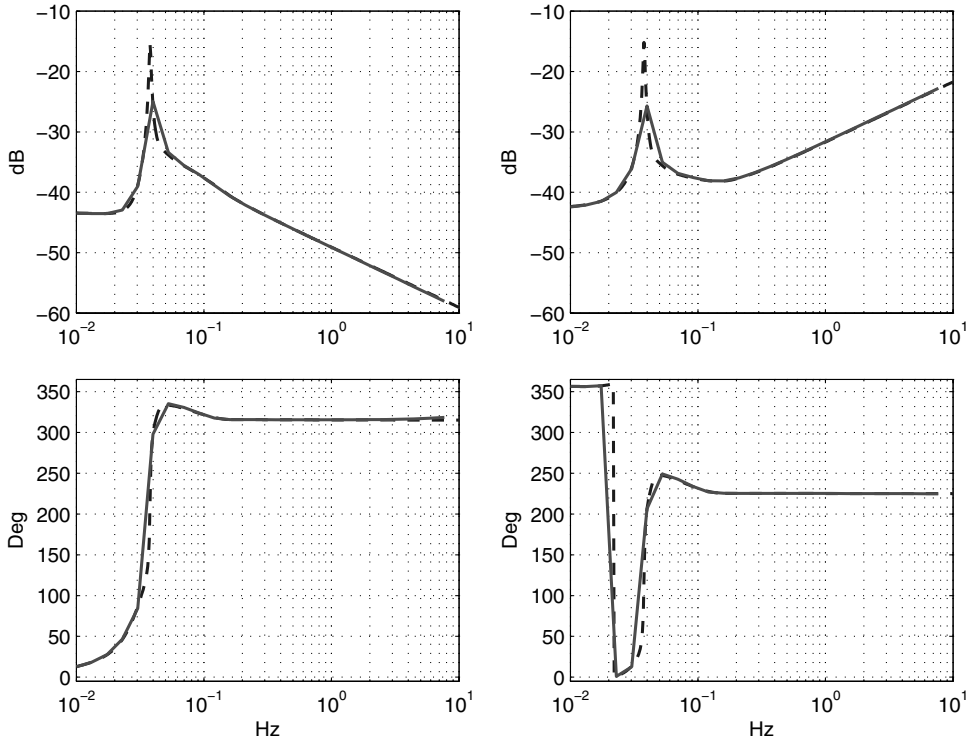

a) Input No. 1 to Output No. 1 b) Input No. 1 to Output No. 2

Fig. 2 Bode plot with a single sample rate: original model (dashed, 256 real states) and empirical (solid).

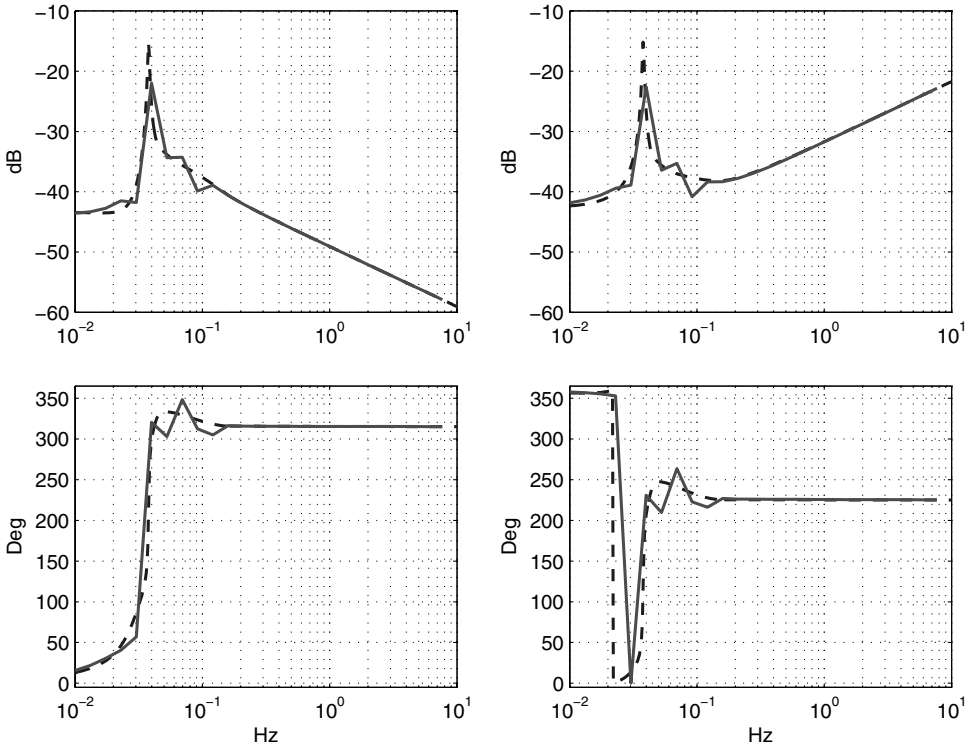

a) Input No. 1 to Output No. 1 b) Input No. 1 to Output No. 2

Fig. 3 Bode plot with double sample rates: original model (dashed, 256 real states) and empirical BROM (solid).

As previously pointed out, it requires on the order of (10^3) snapshots based on a sampling interval of 0.03 to cover both the high frequency of 16 Hz and the low frequency of 0.016 Hz. If we use two sampling intervals, one at 0.03 as before but the other, say, 10 times as large, we may be able to trim down the size of the number of snapshots required. The data matrices remain the same. Basically, now half of the columns of $\mathcal{X}$ in Eq. (8) and of $\mathbf{Y}$ in Eq. (15) are sampling at a high rate and the other half at a low rate. The balancing and reduction scheme for BROM remains unchanged. Hereafter, we present the results.

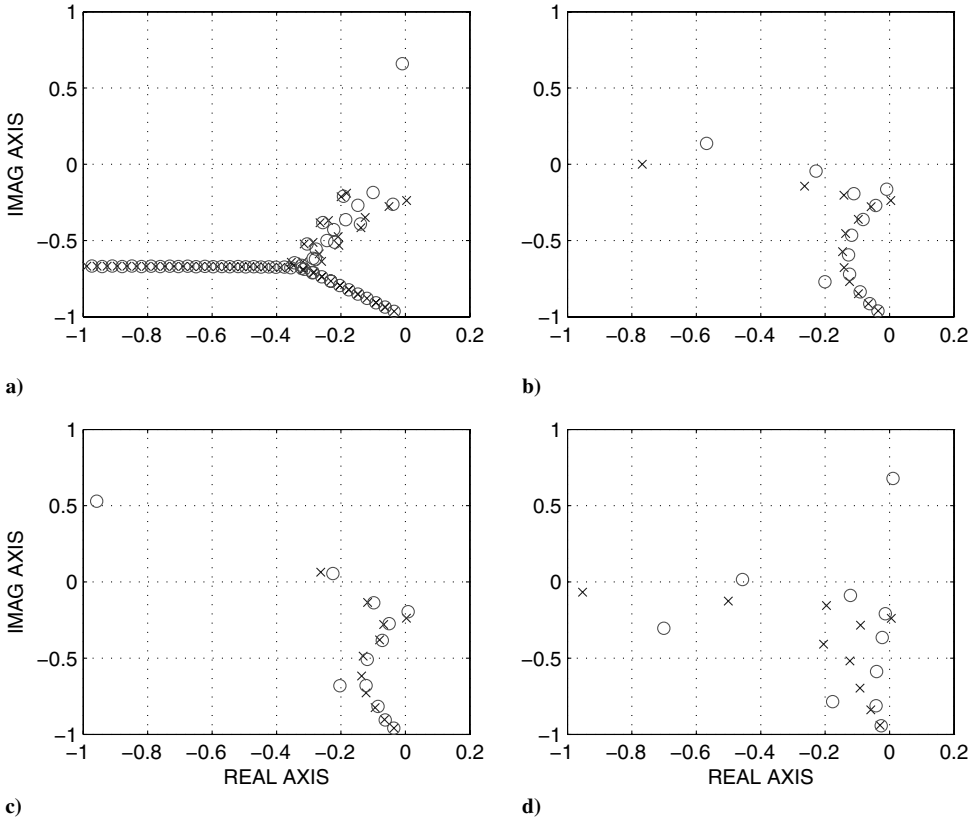

Fig. 4 Pole-zero maps (upper-half *Z* plane only): a) original model, b) BROM with 26 states and 2000 snapshots, c) BROM with 21 states and 2000 snapshots, d) BROM with 26 states and 100 snapshots.

Figure 3 shows the in-channel and cross-channel Bode plots for the two sample rates. The number of snapshots has been dramatically reduced. The way the data is presented remains the same as in Fig. 2. For convenience, we have wrapped the phase plots so that the curves remain in the principal domain from 0 to 360 deg. In sampling, we use 50 snapshots corresponding to the high sampling rate of 0.03 and another 50 snapshots corresponding to the low sampling rate of 0.3. The frequency range targeted is from 10^{-2} to 10^{1}. This range is considered adequate to capture the input–output dynamics of interest. The agreement shown between the two sets of curves are fairly good, suggesting that the order of the BROM is adequate.

For additional insight into the BROM behavior, we provide the pole-zero maps of four cases of interest. Because of symmetry, Fig. 4 shows only the upper-half plane poles (X) and zeros (○) near the imaginary axis. This is the region that displayed sensitivity to the sampling parameters used to obtain the BROM. Figure 4a shows the pole-zero distribution of the original model (256 real states). There are many pole-zero cancellations, and some important high-frequency poles and zeros are not captured in the plotting scale. Fiures. 4b–4d correspond to the BROM. Figure 4b shows the distribution based on 26 complex states. The sampling interval is 0.03 and 2000 snapshots are used. Figure 4c shows the distribution with the same sampling interval and number of snapshots but the number of states is reduced to 21. Figure 4d shows the distribution with two sampling intervals, with 50 snapshots sampled at 0.03 and the other 50 snapshots sampled at 0.3; 26 complex states are used. The Bode plots for all panels except Fig. 4c are shown in Figs. 2 and 3. With 21 states, the gain and phase perform quite poorly, especially for the cross-channel gain and phase. Inspecting Fig. 4 and comparing Figs. 4c and 4d suggests that certain important poles are not captured. Note that the balancing technique tends only to preserve the original modes near the imaginary axis.

V. Conclusions

We use the Poiseuille channel flow stability problem that inputs wall pumping-and-suction control and outputs wall shear stress measurements for our empirical balanced model reduction study. We develop a novel algorithm based on a direct decomposition of the discrete Hankel matrix. The algorithm serves as a generalized balanced POD scheme for input–output model reduction, which suits nonlinear systems well (no adjoint equation is necessary) and is especially convenient and computationally efficient for a small number of snapshots.

Using a large number of snapshots to benchmark the performance of the BROM, the evaluation results include the reconstruction of the neutral stability curve based on the reduced-order system and a comparison of the input-to-output transfer functions of the BROM against the original model (in gain-phase and pole-zero plots). Somewhat contrary to the common notion that only a few POD basis functions are sufficient, this problem requires 52 real states to achieve a good agreement between the original and the reduced system. Moreover, the sampling interval size is restricted by the high-end frequency governed by the input–output structure rather than the low frequency of the dynamics of interest.

For computational efficiency, especially for CFD-based models, it is highly desirable to reduce the number of snapshots required for maintaining a reasonable level of performance. We investigate a large number of gain-phase and pole-zero plots by changing the sampling parameters. We conclude that a single sampling rate is unable to achieve good performance for a relatively small number of snapshots, that is, on the order of 10–100, and certainly not 1000. We demonstrate that sampling at two interval sizes allows the total number of snapshots to be reduced dramatically, from a couple of thousand snapshots to 100 snapshots. The dual sampling frequencies serve to patch together the high and low ends.

Acknowledgments

The work was supported by the Air Force Office of Scientific Research under contract FA9550-05-C-0031. Any opinions, findings, conclusions, or recommendations expressed here are those of the authors and do not necessarily reflect the views of the Air Force Office of Scientific Research. The authors would like to thank John

Kim for bringing to our attention the work of C.W. Rowley, which has been demonstrated in our results to be a useful empirical balanced model reduction technique.

References

[1] Joshi, S. S., Speyer, J. L., and Kim, J., "A Systems Theory Approach to the Feedback Stabilization of Infinitesimal and Finite-Amplitude Disturbances in Plane Poiseuille Flow," *Journal of Fluid Mechanics*, Vol. 332, 1997, pp. 157–184.

[2] Joshi, S. S., Speyer, J. L., and Kim, J., "Finite Dimensional Optimal Control of Poiseuille Flow," *Journal of Guidance, Control, and Dynamics*, Vol. 22, No. 2, 1999, pp. 340–348.

[3] Mahajan, A., Dowell, E., and Bliss, D., "Eigenvalue Calculation Procedure for an Euler/Navier–Stokes Solver with Applications to Flows over Airfoils," *Journal of Computational Physics*, Vol. 97, 1991, pp. 398–413.
doi:10.1016/0021-9991(91)90006-7

[4] Carlson, H. A., Thirunavukkarasu, V., Speyer, J. L., and Or, A. C., "Closed-Loop Control of Airfoil Lift," AIAA Paper 2006-3018, 2006.

[5] Drazin, P. G., and Reid, W. H., *Hydrodynamic Stability*, Cambridge Univ. Press, Cambridge, England, U.K., 1982, pp. 153.

[6] Holms, P., Lumley, J. L., and Berkooz, G., *Turbulence, Coherent Structures, Dynamical Systems and Symmetry*, Cambridge Univ. Press, Cambridge, England, U.K., 1998.

[7] Moore, B., "Principal Component Analysis in Linear Systems," *IEEE Transactions on Automatic Control*, Vol. 26, No. 1, Feb. 1981, pp. 17–31.
doi:10.1109/TAC.1981.1102568

[8] Willcox, K., and Peraire, J., "Balanced Model Reduction via the Proper Orthogonal Decomposition," *AIAA Journal*, Vol. 40, No. 1, 2002, pp. 2323–2330.

[9] Lall, S., Marsden, J. E., and Glavaski, S., "A Subspace Approach to Balanced Truncation for Model Reduction of Nonlinear Control Systems," *International Journal of Robust and Nonlinear Control*, Vol. 12, No. 6, 2002, pp. 519–535.
doi:10.1002/rnc.657

[10] Rowley, C. W., "Model Reduction for Fluids, Using Balanced Proper Orthogonal Decomposition," *International Journal of Bifurcation and Chaos in Applied Sciences and Engineering*, Vol. 15, No. 3, 2005, pp. 997–1013.
doi:10.1142/S0218127405012429

[11] Or, A. C., Speyer, J. L., Kang, S. M., and Kim, J., "Convergence Properties of Different Spectral Approximations for an Infinite Dimensional Input–Output System," *Journal of Fluid Mechanics*, (submitted for publication).